The Astrophysical Journal, 807:71 (12pp), 2015 July 1 doi:10.1088/0004-637X/807/1/71

DYNAMICS OF ON-DISK PLUMES AS OBSERVED WITH THE INTERFACE REGION IMAGING SPECTROGRAPH, THE ATMOSPHERIC IMAGING ASSEMBLY, AND THE HELIOSEISMIC AND MAGNETIC IMAGER

Vaibhav Pant[1], Laurent Dolla[2], Rakesh Mazumder[1,3], Dipankar Banerjee[1,3], S. Krishna Prasad[4], and Vemareddy Panditi[1]
[1] Indian Institute of Astrophysics, Koramangala, Bangalore 560034, India; vaibhav@iiap.res.in
[2] Solar-Terrestrial Center of Excellence, Royal Observatory of Belgium, Avenue Circulaire 3, B-1180 Brussels, Belgium
[3] Center of Excellence in Space Sciences India, IISER Kolkata, Mohanpur 741246, West Bengal, India
[4] Astrophysics Research Centre, School of Mathematics and Physics, Queen's University Belfast, Belfast BT7 1NN, UK
Received 2015 March 23; accepted 2015 May 15; published 2015 July 1

ABSTRACT

We examine the role of small-scale transients in the formation and evolution of solar coronal plumes. We study the dynamics of plume footpoints seen in the vicinity of a coronal hole using the Atmospheric Imaging Assembly (AIA) images, the Helioseismic and Magnetic Imager magnetogram on board the *Solar Dynamics Observatory* and spectroscopic data from the *Interface Region Imaging Spectrograph* (*IRIS*). Quasi-periodic brightenings are observed in the base of the plumes and are associated with magnetic flux changes. With the high spectral and spatial resolution of *IRIS*, we identify the sources of these oscillations and try to understand what role the transients at the footpoints can play in sustaining the coronal plumes. *IRIS* "sit-and-stare" observations provide a unique opportunity to study the evolution of footpoints of the plumes. We notice enhanced line width and intensity, and large deviation from the average Doppler shift in the line profiles at specific instances, which indicate the presence of flows at the footpoints of plumes. We propose that outflows (jet-like features) as a result of small-scale reconnections affect the line profiles. These jet-like features may also be responsible for the generation of propagating disturbances (PDs) within the plumes, which are observed to be propagating to larger distances as recorded from multiple AIA channels. These PDs can be explained in terms of slow magnetoacoustic waves.

Key words: Sun: corona – Sun: oscillations – Sun: UV radiation

Supporting material: animations

1. INTRODUCTION

Coronal plumes, extending as bright narrow structures from the solar chromosphere into the high corona are mostly rooted in coronal holes (CHs) or their neighborhood (van de Hulst 1950; Saito 1958, 1965; DeForest et al. 2001). They are plasma density enhancements in the low and extended corona aligned along the magnetic field (Velli et al. 2011; Wilhelm et al. 2011). Plume footpoints are typically 4″ wide and plumes expand rapidly with height (DeForest et al. 1997). Raouafi et al. (2006, 2007) showed that plumes are more than five times denser than the interplume regions at the base of the corona. Multi-wavelength UV–EUV imaging and spectral observations from the *Solar and Heliospheric Observatory* (*SOHO*), the *Solar TErrestrial RElations Observatory* (*STEREO*), and the *Solar Dynamic Observatory* (*SDO*) allowed us to study the formation and evolution of plumes (see review by Wilhelm et al. 2011). Plumes are difficult to observe in low-latitude CHs because of the bright foreground and background emission (Wang & Muglach 2008). The low-latitude plumes appear to be similar to their polar counterparts (Tian et al. 2011c). Saito & Tanaka (1957) first pointed out the association of polar plumes with magnetic flux concentrations. It was also revealed by many studies that polar plumes arise from unipolar magnetic regions associated with the super-granular network boundaries (Harvey 1965; Newkirk & Harvey 1968; Fisher & Guhathakurta 1995; DeForest et al. 1997, 2001; Young et al. 1999) Coronal plumes can be formed due to magnetic reconnection of newly emerging magnetic flux with the pre-existing dominant unipolar fields (Grappin et al. 2011), which can further lead to localized heating (Wang & Sheeley 1995). Raouafi et al. (2008) and Raouafi & Stenborg (2014) discovered that coronal jets are the precursors of plumes.

Ofman et al. (1997) reported quasi-periodic variations in polar CHs and conjectured compressive waves to be responsible for them. Quasi-periodic brightness variations in plumes have been observed with Extreme Ultraviolet Imaging Telescope (EIT) by DeForest & Gurman (1998). They found the presence of propagating disturbances (PDs) in several plumes with periods between 10 and 15 minutes and speeds between 75 and 150 km s^{-1} in the height range from 0.01 R_s to 0.2 R_s. They conjectured such PDs to be compressive waves. A number of studies followed, reporting such oscillations in plumes, interplumes, and CHs, using spectroscopic data obtained with the Coronal Diagnostic Spectrometer (CDS) and Solar Ultraviolet Measurements of Emitted Radiation (SUMER) on board *SOHO* and the Extreme ultraviolet Imaging Spectrometer (EIS) on board *Hinode* (Banerjee et al. 2000, 2001, 2009; O'Shea et al. 2006; Gupta et al. 2009). Using extreme ultraViolet (EUV) observations from *STEREO*, McIntosh et al. (2010) analyzed several plume structures and suggested that PDs along polar plumes could be due to the collimated high-speed plasma jets that have similar properties to slow magnetoacoustic waves. Further, they conjectured that these jets could be responsible for loading a significant amount of heated plasma into the fast solar wind. Indeed, recent high-resolution observations have revealed jet-like flows at the bases of plumes (Raouafi & Stenborg 2014) and at network boundaries in CHs (Tian et al. 2014). The plume formation

and dynamics are still a matter of debate related to the broader issue of wave propagation, plasma jets, and their role in the acceleration of the fast solar wind.

To understand the nature of the source regions of plumes and the PDs, we study the footpoints of an on-disk plume adjacent to a CH as seen in the Atmospheric Imaging Assembly (AIA) EUV coronal images (Lemen et al. 2012) and in the Helioseismic and Magnetic Imager (HMI) magnetogram (Schou et al. 2012) on the *SDO* and simultaneously with the *Interface Region Imaging Spectrograph* (*IRIS*; De Pontieu et al. 2014). Combining imaging and spectroscopic observations, we focus on the dynamics of this plume. We show that the jet-like features (termed "jetlets") load mass to the plumes and can also be responsible for the generation of the PDs as observed at greater heights.

2. DATA ANALYSIS AND RESULTS

2.1. Observation and Data Reduction

Observational data were obtained from *IRIS*, AIA, and HMI instruments from 16:26 UT to 17:51 UT on 2014 July 12. We used AIA passbands at 193, 171, and 1600 Å and HMI line-of-sight (LOS) magnetograms. We used standard AIA prep routines to produce level 1.5 images. *IRIS* data are taken in sit-and-stare mode with the slit centered at 239″, −559″ pointing adjacent to a coronal hole. This dataset has three spectral lines, namely C II 1335.71 Å, Si IV 1402.77 Å, and Mg II k 2796 Å. We use Si IV 1402.77 Å for this study. Slit-jaw images (SJIs) were available only with the 1330 Å filter. We have used *IRIS* level 2 processed data which are corrected for dark current, flat field, and geometrical corrections etc. The cadence of 1330 Å SJIs and spectra was ∼5 s with a pixel size of 0.″166. AIA and HMI images were de-rotated before AIA 1600 Å images were co-aligned with *IRIS* SJIs 1330 Å using cross-correlation. Figure 1 shows the plume as seen in various AIA channels, *IRIS* 1330 Å SJI, and HMI LOS magnetogram. The magnetogram (Figure 1(b)) shows that the plume is dominated by negative-polarity magnetic field marked with red contours (−50 G). We made an Movie 1 (84 minutes, available online) with HMI LOS magnetogram images; it shows the evolution of negative and positive flux with time. In the movie, red and green contours represent magnetic field strengths of −50 and 20 G, respectively.

Figure 1 clearly shows that the *IRIS* slit is crossing the footpoints of the plume. We extrapolate the coronal magnetic field with a potential field approximation, using the LOS magnetic field observed by HMI as the boundary condition at the photosphere (Figure 2). We select a large field of view (FOV) around this plume structure to approximately satisfy the flux balance condition. This FOV magnetogram is projected to disk center correcting for the difference between normal and LOS values, and we compute the potential field in a 3D box (Gary 1989) encompassing the plume structure.

We trace field lines having footpoints in strong magnetic patches ($|B_z| > 25$ G). In Figures 2(a) and (b), they are overlaid on the boundary magnetogram along with contours (±25 G). Most of the field lines from the magnetic regions are open (yellow). The shapes of the two major open-field structures associated with the strong negative magnetic patches are consistent with the funnel structure of the plume originating from the network boundary, as revealed from the AIA images (Figures 1(c) and (d)). However, only the northernmost structure appears bright in the AIA images at the time of the observations. Note that the difference in the orientation is due to projection, which is corrected in this model. It is also noted that the plume originates from the network boundary, as revealed from *IRIS* SJIs (Figure 1(a)).

Apart from these open field lines, low-lying field lines (blue) connect the weak field regions in the immediate neighborhood of the main plume structure. Movie 1 shows the continuous emergence of positive flux followed by flux cancellation. Reconciling the model of Shibata et al. (1994), the open-dipped field lines at the edges of the plume, in a dynamical scenario, facilitate continuous reconnection with the neighboring closed field lines to supply heat and energy for sustaining the plume.

2.2. Spectroscopic Analysis

We have focused on the dynamics of two footpoints (negative polarity) as marked by a triangle and square (at "Y" positions −546″ and −564″ respectively) in Figure 1. We study the time evolution of this small region as seen in *IRIS* Si IV 1402.77 Å spectral profiles. At first, a single Gaussian fit is performed on the weighted averaged (three pixels along the slit and three in time) spectral profile. We average the spectral profiles to increase the signal-to-noise ratio, using error bars as calculated by *iris_pixel_error.pro* as weights. From the single Gaussian fit we derive peak intensity, Doppler shift, line width, and asymmetry coefficient (see Figure 3). We use the median of the centroid of the fitted Gaussians as the rest wavelength to estimate the Doppler velocity. The evolution of the spectral profile at these two positions as a function of time is shown in Movie 2 (available online). In this movie *IRIS* 1330 Å SJIs are also included to show the jet-like features at network boundaries. To analyze the non-Gaussian aspect of the spectral profiles, we use the coefficient of asymmetry defined in Dolla & Zhukov (2011). However, contrary to what was done in that work, we do not normalize by the error bars of spectral intensities, because we are interested here in quantifying the asymmetry and not in assessing its statistical significance. The coefficient of asymmetry therefore provides the percentage of area in the profile that deviates from the fitted single Gaussian, according to the pattern defined by the following formula:

$$A = \frac{1}{I_0}\sum_k \epsilon(\lambda)\cdot \mathrm{sgn}\big(\Delta_k(\lambda)\big)\cdot \Delta_k(\lambda), \tag{1}$$

where λ is the wavelength, I_0 is the total intensity in the spectral line and $\Delta(\lambda) = s_k(\lambda) - f_k(\lambda)$ is the difference between the spectrum $s_k(\lambda)$ and the fitted Gaussian $f_k(\lambda)$, which are discretized on bin k. The contribution factor $\epsilon(\lambda)$ is defined as follows:

$$\epsilon(\lambda) = \begin{cases} -1 & \text{if } \lambda \in \big[\lambda_0 - 2\sigma;\ \lambda_0 - \sigma\big) \\ 1 & \text{if } \lambda \in \big[\lambda_0 - \sigma;\ \lambda_0\big) \\ -1 & \text{if } \lambda \in \big(\lambda_0;\ \lambda_0 + \sigma\big] \\ 1 & \text{if } \lambda \in \big(\lambda_0 + \sigma;\ \lambda_0 + 2\sigma\big] \\ 0 & \text{otherwise,} \end{cases} \tag{2}$$

where λ_0 is the center and σ the half-width at $1/\sqrt{e}$ of the fitted Gaussian. The sign of the coefficient of asymmetry indicates in which wing of the profile most imbalance is present (negative and positive on the blue and red wings, respectively). Another

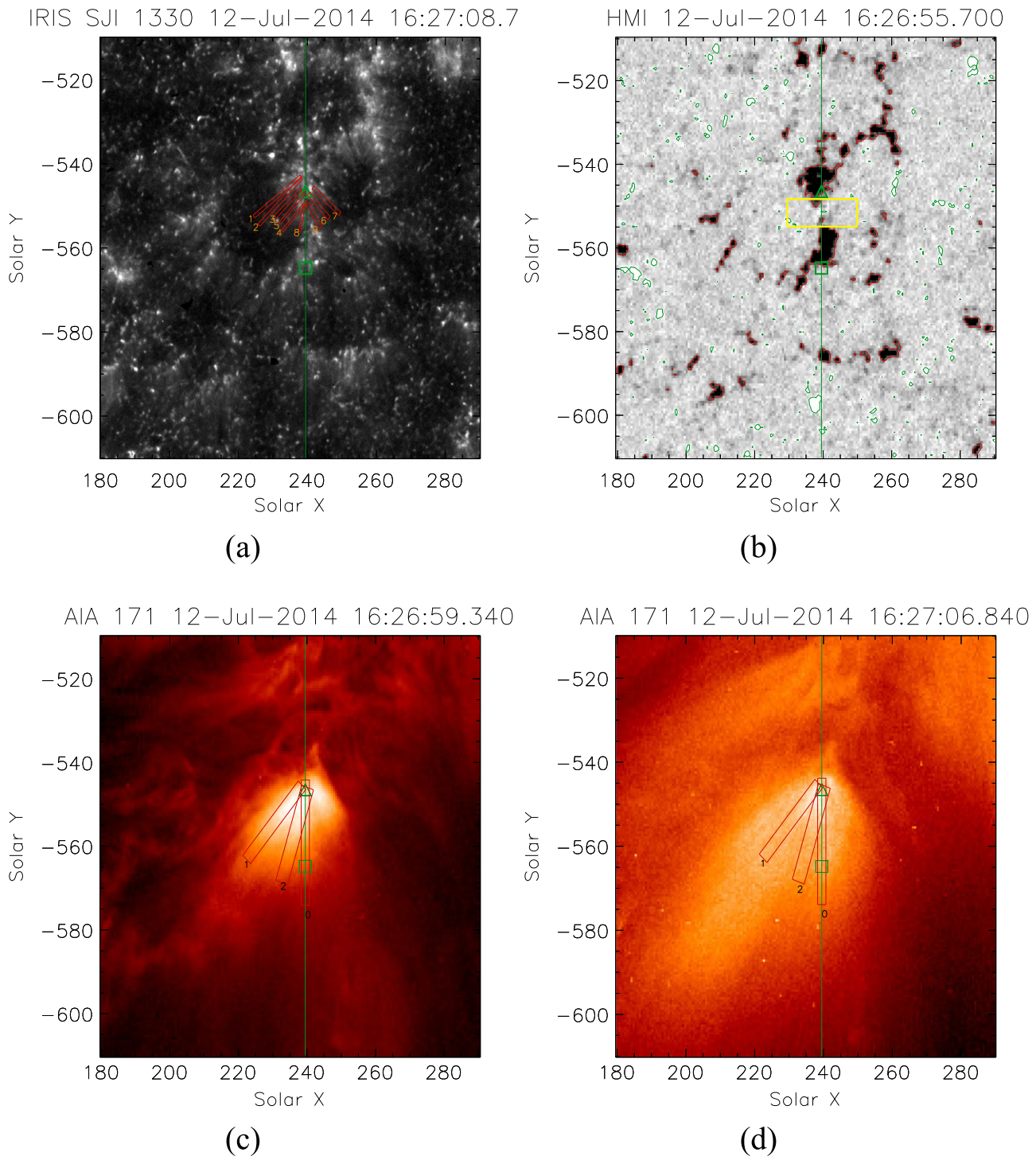

Figure 1. (a) *IRIS* 1330 Å SJI represents our region of interest (ROI), covering an on-disk plume adjacent to a coronal hole. Nine artificial slices are placed for further analysis. (b) HMI LOS magnetogram. The yellow box represents the region used for calculating the positive flux (see Figure 5). (c) AIA/SDO 171 Å image overplotted with three artificial slices used to create time–distance maps (see Figure 6). (d) Same as (c) for AIA/SDO 193 Å image. The vertical green line on each image represents the position of the *IRIS* slit. The green triangle is the location where we study the variation of different parameters of the Si IV 1402.77 Å line (see Figure 5). The green triangle and square symbols represent the "Y" positions along the *IRIS* slit used to analyze spectra (see Figure 4 and Movie 2).

(An animation of this figure is available.)

method of quantifying the profile asymmetry is the red–blue (RB) asymmetry method. The RB technique has been widely used in both optically thick (e.g., in Hα, Madjarska et al. 2009; Huang et al. 2014) and optically thin (e.g., De Pontieu et al. 2009; Tian et al. 2011b) spectral-line analysis.

Figure 4 shows spectral profiles at different instances (as marked in Figure 3) along the slit. We find that the spectral profiles are significantly non-Gaussian with two or more components present. We fit the spectral profiles at these instances with a single Gaussian (shown in orange) and double

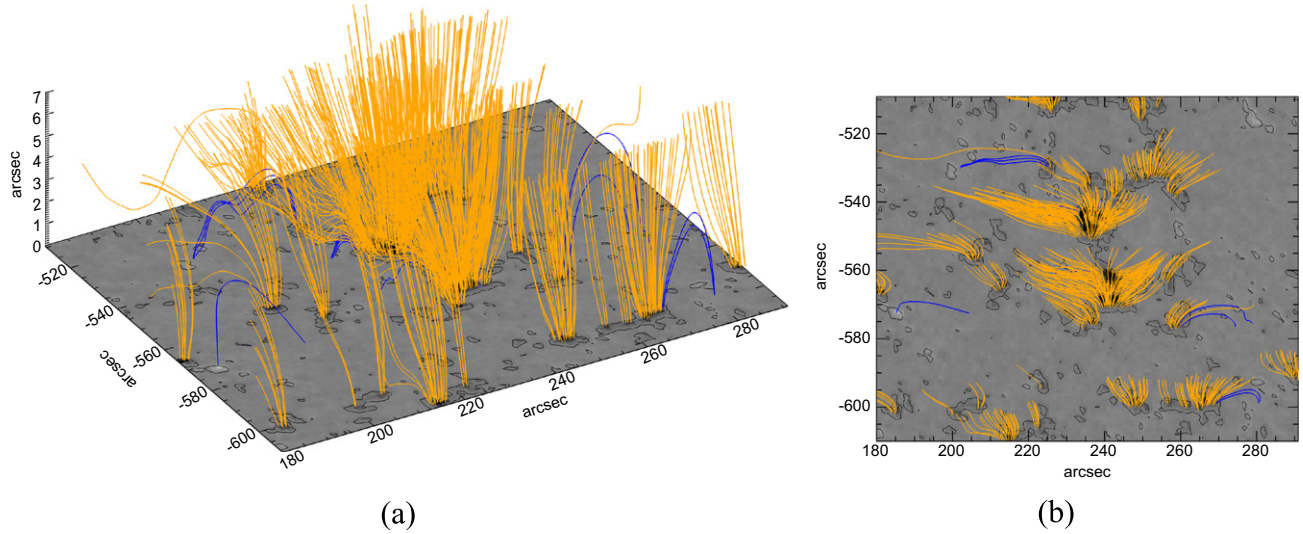

Figure 2. (a) 3D view of extrapolated field lines. (b) 2D view of extrapolated field lines.

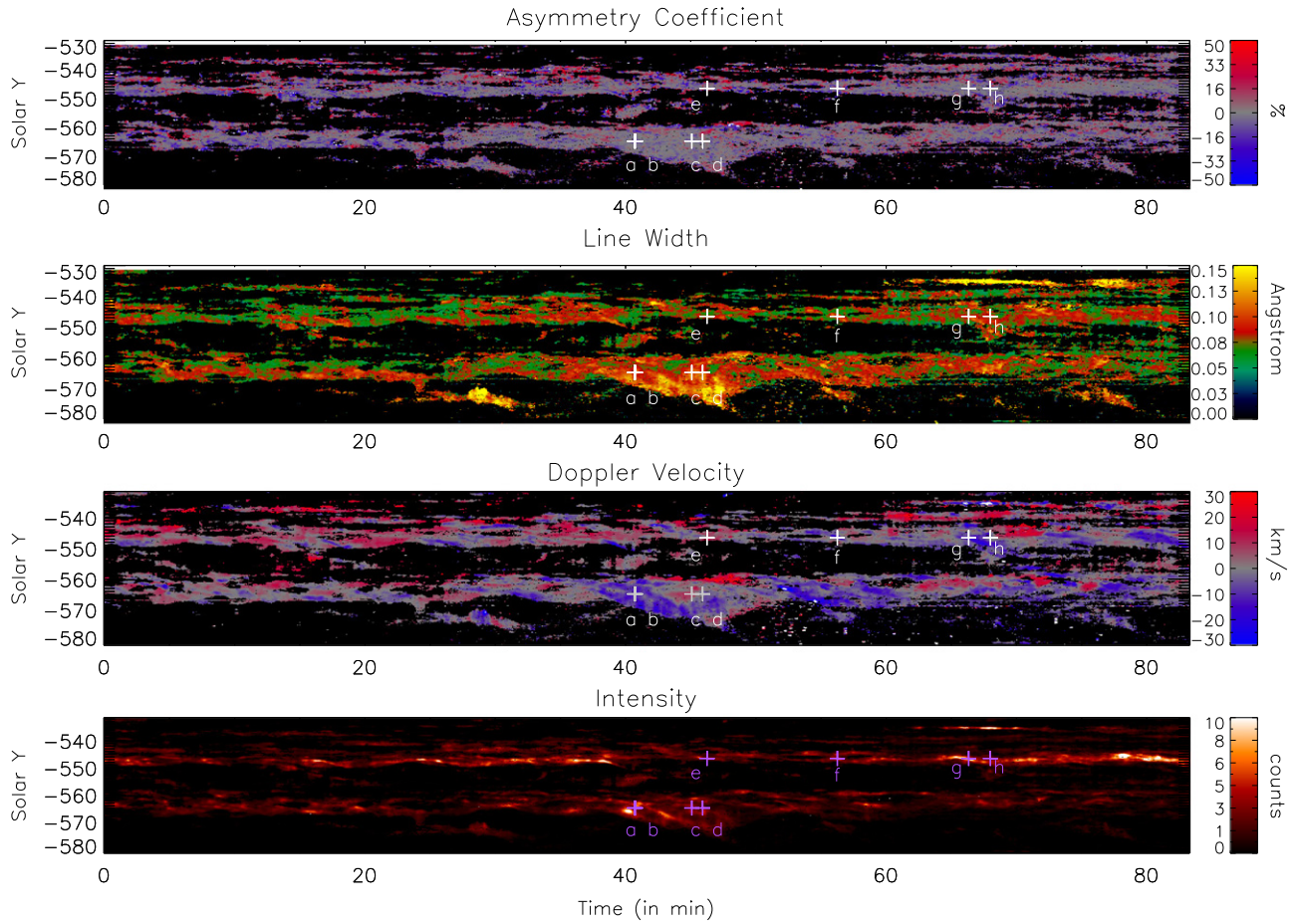

Figure 3. Time evolution of peak intensity, Doppler velocity, line width, and asymmetry coefficient as derived from single Gaussian fitting over Si IV 1402.77 Å spectra. Positions marked as (a)–(h) are used to show individual spectral profiles. (See Figure 4.)

(An animation of this figure is available.)

Gaussian (in green). Spectra averaged during the first 20 minutes of observations at the same "Y" positions are shown in blue. Both components of the double Gaussian are shown in gray. We observe both blueward and redward asymmetries at different instances (see Figure 4). The large asymmetry and double Gaussian behavior of the spectral profile indicates the presence of flows at these instances. Such behavior can also be attributed to waves (Verwichte et al. 2010) but we can discard this interpretation in our observations because the associated fluctuations in intensity are

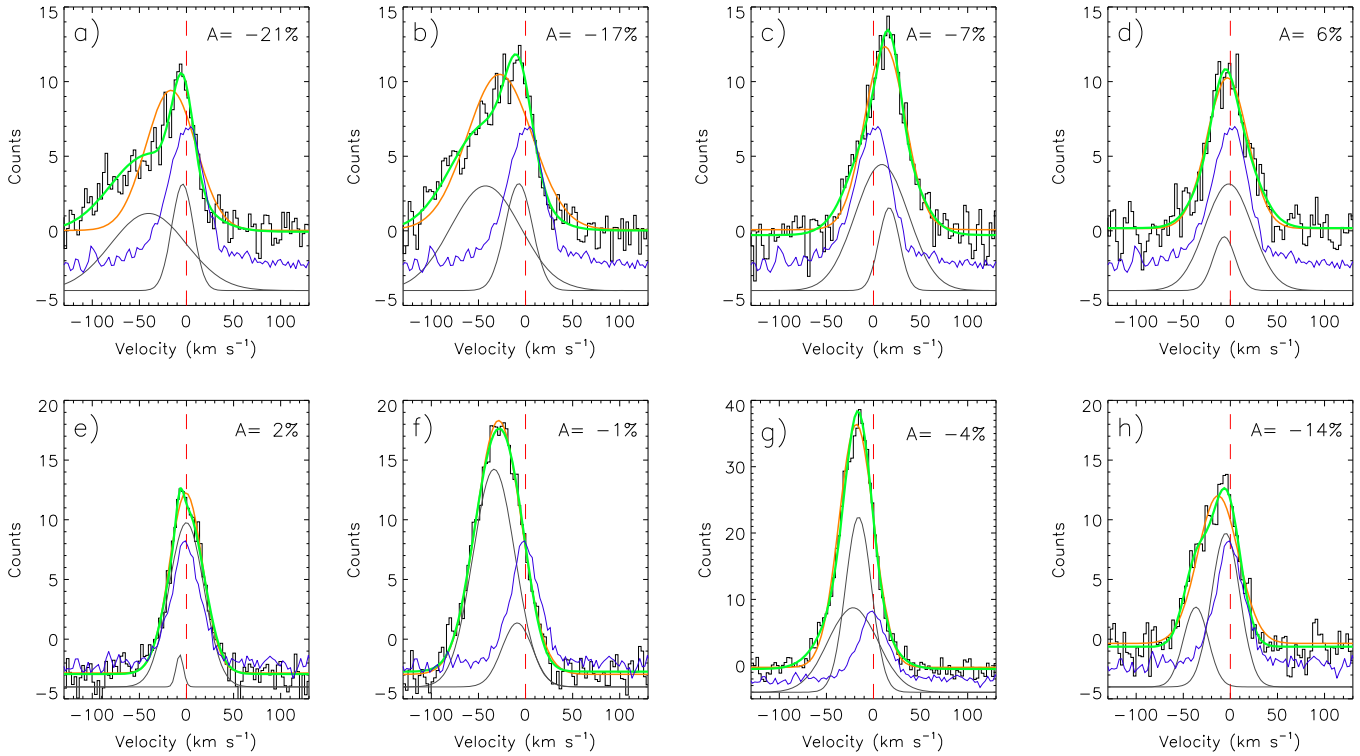

Figure 4. Representative line profiles at different positions as marked in Figure 3. Orange and green curves represent the best-fit single Gaussian and double Gaussian over spectra. Two components of the double Gaussian fit are shown in gray and shifted to the bottom for better visiblity. The blue curve represents the average spectrum over the first 20 minutes of the observation at the respective positions.

too large to correspond to linear waves only (see Figure 5). Non-Gaussian behavior is present on several occasions during the time of observation of *IRIS* at the positions marked by the triangle and square in Figure 1 (see Movie 2 online). *IRIS* 1330 Å SJIs show the presence of several small-scale jets throughout the time of observation at these two positions. Reconnection jets cause enhancements at the line wings, which lead to large asymmetries, larger line width, greater intensity, and large Doppler shift. The redshift in spectra could be a projection effect as the plume is close to the south pole. Besides this the redshifts may indeed imply that at least part of the material is falling back. This is consistent with Figure 5 where the brightenings are associated with strong blueshifts, with progressive evolution not only toward zero but also redshifts (i.e., velocities slightly positive). There is probably a combination of both blueshifts and redshifts during this recovery phase.

In Figure 5 we show the wavelet analysis of spectral intensity, Doppler shift, and line width at the plume footpoint marked by a triangle (see Figure 1). The missing values in the left panel of Figure 5 correspond to the positions where a single Gaussian could not be fitted due to low counts. The green stars in Figure 5 represent the instances we have chosen to show individual spectral profiles (see Figures 4(e)–(h)). In the right panel global wavelet power peaks at 15.6 and 7.1 minutes for intensity, 26.2 and 7.1 minutes for Doppler velocity, and 11 and 17 minutes for line width. A small peak ∼16 minutes in global wavelet power of Doppler velocity is also present. The horizontal dashed line is the cutoff above which edge effects come into play; thus periods above the dashed line cannot be trusted. The dotted line marks the 99% significance level for a white noise process (Torrence & Compo 1998).

It is quite evident from Figure 5 that the instances of the intensity peaks correspond to instances of large Doppler shifts and line widths and the flux cancellation of emerging positive flux. Movie 1 shows the evidence of a positive-polarity field around the dominant negative polarity. Cancellation of positive polarity at the edges of dominant negative polarity (region enclosed in a yellow box in movie 1) leads to the formation of reconnection jets that are characterized by intensity enhancement in spectra and apparent outflows in *IRIS* 1330 Å SJIs.

2.3. Imaging Analysis

In order to compare dynamics at the transition region (as seen from *IRIS*) and the corona (as seen from AIA), we create smooth background-subtracted time–distance maps of AIA 171 Å and AIA 193 Å for the artificial slice 0 (see Figures 1(c) and (d)) co-spatial with the *IRIS* slit shown in green in Figure 1. We choose the width of the slice to be four pixels. We average along the width of the slice to increase signal to noise. Resulting time–distance maps are shown in Figure 6 (left panel). We observe quasi-periodic alternate bright and dark ridges. We fit the ridges with a straight line as done in Kiddie et al. (2012) and Krishna Prasad et al. (2012). We isolate a ridge and estimate the position of maximum intensity. We then fit the points of maximum intensity with a straight line, and thus the mean value of slope and error bars are estimated. The slope of the straight line gives an estimate of the speed of the PDs. Since we are interested in the average behavior of the PD, we take the mean of the speeds of all the ridges, and therefore some of the ridges in AIA 171 Å seem to be more inclined than overplotted straight lines. We find the average velocity of PDs is 51 ± 3 and 66 ± 8 km s^{-1} in AIA 171 and 193 Å respectively.

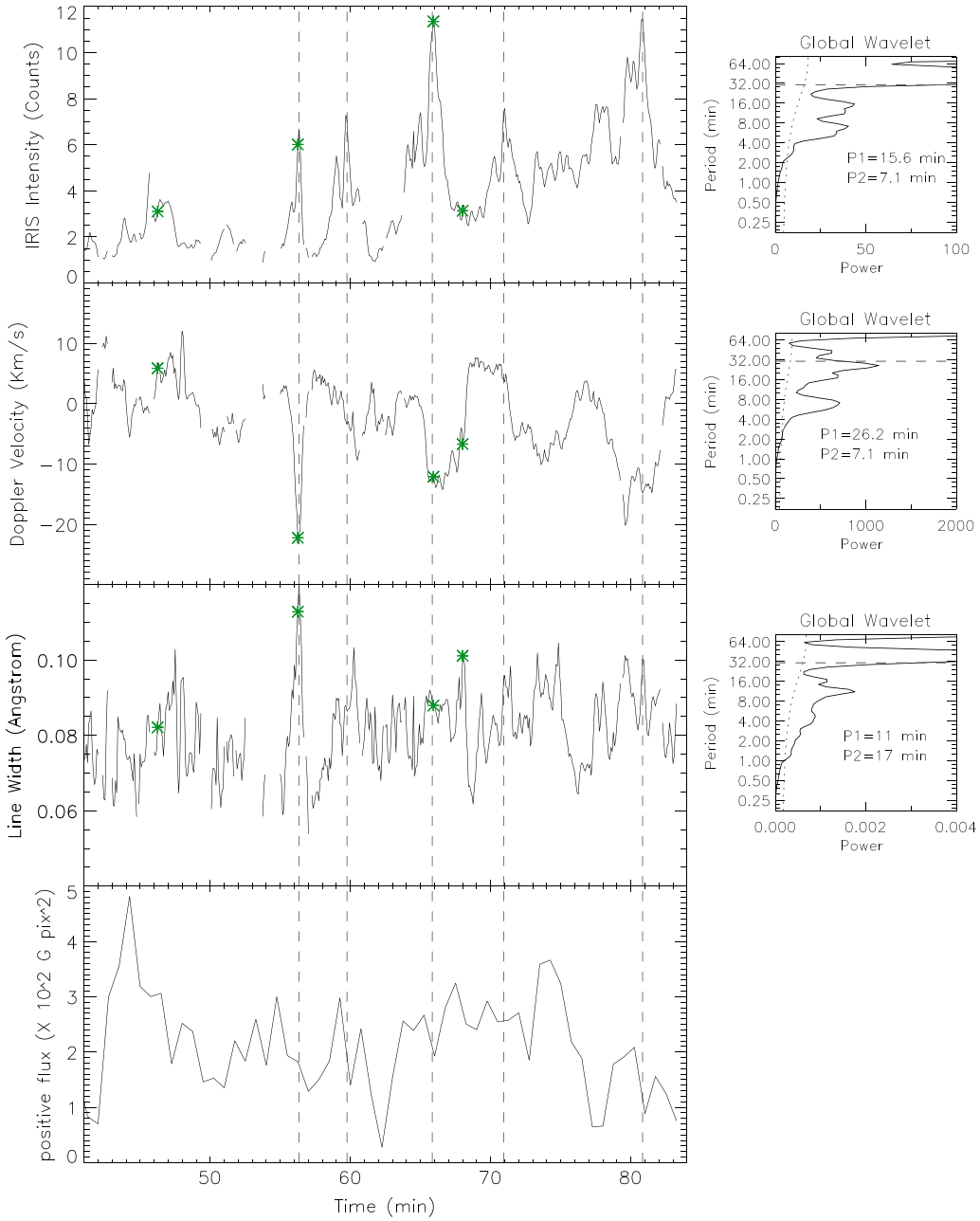

Figure 5. Left: time variation of the Si IV line parameters at the triangle location (*IRIS*) and of the positive magnetic flux within the yellow box (HMI), as shown in Figure 1. The green stars identify the times at which we show individual spectral profiles in Figure 4. Right: corresponding global wavelet power spectra. The 99% significance levels are overplotted with dotted lines. The first two significant periods are indicated.

We carry out a similar analysis for two artificial slices marked as 1 and 2 in Figures 1(c) and (d) for AIA 171 and 193 Å, respectively. The slices are placed by looking at the direction of propagation of significant PDs in unsharp mask images. The widths of slices 1 and 2 are chosen to be 5 and 6 pixels respectively. Corresponding time–distance maps with best-fit overplotted ridges for slices 1 and 2 are shown in Figure 6 (middle and right panels respectively). We note that the velocity is higher in the hotter channel (AIA 193 Å) and the ratio between the velocity observed in AIA 193 and 171 Å is 1.29 ± 0.23, 1.23 ± 0.1, and 1.32 ± 0.07 (as compared to the theoretical value of 1.25 if the PDs are magnetoacoustic waves) for slices 0, 1, and 2 respectively.

We also estimate the velocities of PDs in slices 0, 1, and 2 using a cross-correlation method as done in Kiddie et al. (2012). We isolate individual ridges and estimate the time lag using cross-correlation between two positions. The velocity of the ridge is estimated by dividing the distance between two positions by the time lag. Thus, we compute the velocities of several ridges, and their mean value and standard deviation are estimated. Mean velocities and error bars (standard deviation for cross-correlation) using two different methods for slices 0, 1, and 2 are summarized in Table. 1.

Since the velocity is higher in the hotter channel (AIA 193 Å) using two different methods, we believe that these are propagating slow magnetoacoustic waves. We carry out a

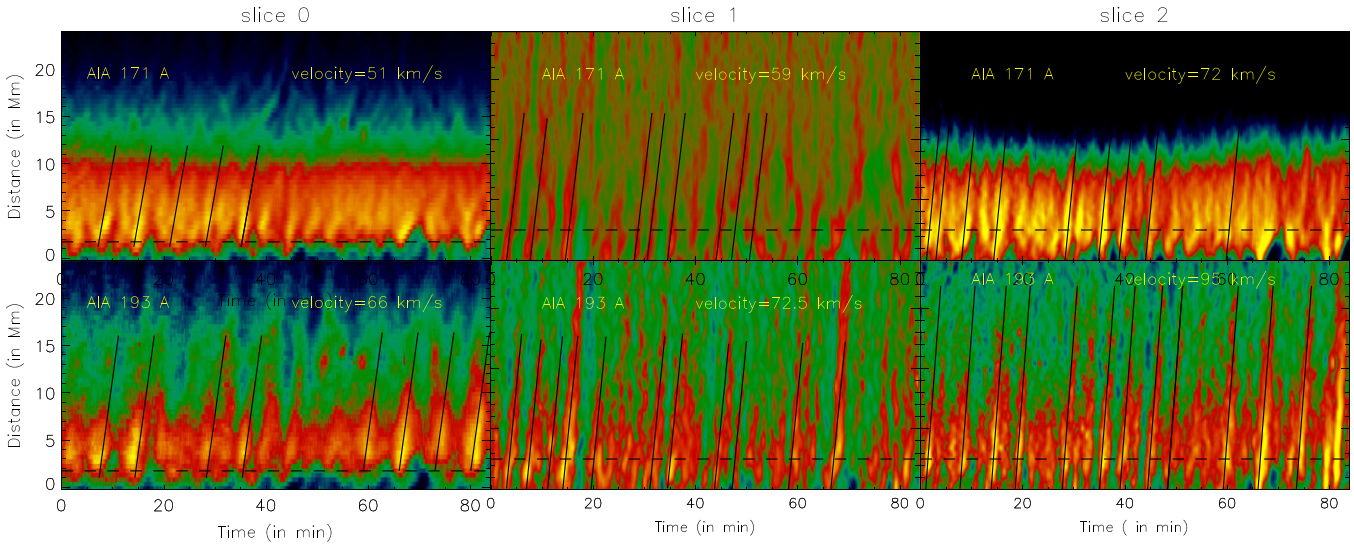

Figure 6. (Top panel) Left: smooth background-subtracted x–t map of slice 0 as shown in Figure 1(c) for AIA 171 Å. Ridges are overplotted with the best-fit straight line. Middle: smooth background divided x–t map of slice 1 for AIA 171 Å. Ridges are overplotted with the best-fit straight line. Right: same as (a) for slice 2. The dashed black line represents the position used for wavelet analysis as shown in Figure 7. (Bottom panel) Same as the top panel for AIA 193 Å.

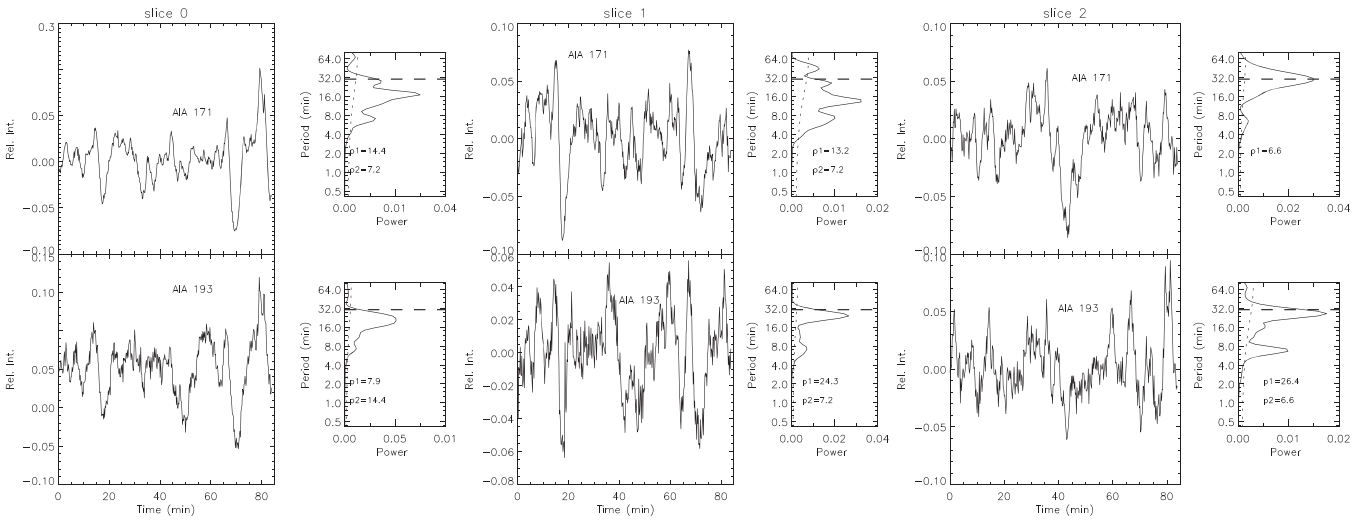

Figure 7. (Top panel) Left: detrended light curves corresponding to black dashed lines for slice 0 as shown in Figure 6 left panel. Corresponding global wavelet plots are shown with the first two dominant periods. Middle: same as the left panel for slice 1. Right: same as the left panel for slice 2. (Bottom panel) Same as Top panel for AIA 193 Å.

Table 1
Velocity of PDs Using Two Different Methods of Ridge Fitting

Slice	Channel	Velocity (km s^{-1})	
		Using Best-fit Straight Line	Using Correlation
0	AIA 171 Å	51 ± 3	61 ± 12
	AIA 193 Å	66 ± 8	81 ± 11
1	AIA 171 Å	59 ± 3	60 ± 14
	AIA 193 Å	72.5 ± 1	80 ± 18
2	AIA 171 Å	72 ± 5	63 ± 10
	AIA 193 Å	95 ± 3	83 ± 25

wavelet analysis at positions marked with dashed lines in Figure 6 (left panel). We find that there exist at least two dominant significant periodicities close to the footpoint of the plume (see global wavelet power plot in Figure 7). We choose the significance level to be 99% for a white noise process. We find that the periodicities in intensity in AIA 171 and 193 Å at slice 0 are similar to those in *IRIS* Si IV 1402.77 Å peak intensity (see Figure 5 top panel). We also find that the periodicity of 7.2 minutes is present in AIA 171 Å, AIA 193 Å, and *IRIS* spectral intensity, which suggests that the quasi-periodic reconnection jet outflows could be responsible for quasi-periodic PDs seen in AIA 171 and 193 Å.

For slices 1 and 2 the rows marked with dashed lines in Figure 6 are used in the wavelet analysis (Figure 7). We find the two dominant periodicities of 13.2 and 7.2 minutes (24.3 and 7.2 minutes) and 17.1 and 6.6 minutes (26.4 and 6.6 minutes) in AIA 171 Å (193 Å) for slices 1 and 2, respectively (see Table 2).

We also carry out the wavelet analysis at other positions (10 and 15 Mm in the x–t map). The results are summarized in Table 2.

Table 2
Dominiant Periodicity Using Wavelet Transform

Slice	Distance Along Slice (Mm)	AIA 171 Å		AIA 193 Å	
		*P*1 (minutes)	*P*2 (minutes)	*P*1 (minutes)	*P*2 (minutes)
0	2	14.4	7.2	7.9	14.4
	5	5.6	9.4	7.2	12.1
	10	22.2	6.6	13.2	7.2
	15	12.1	7.2	12.1	7.2
1	2.5	13.2	7.2	24.3	7.2
2	2.5	6.6	⋯	26.4	6.6

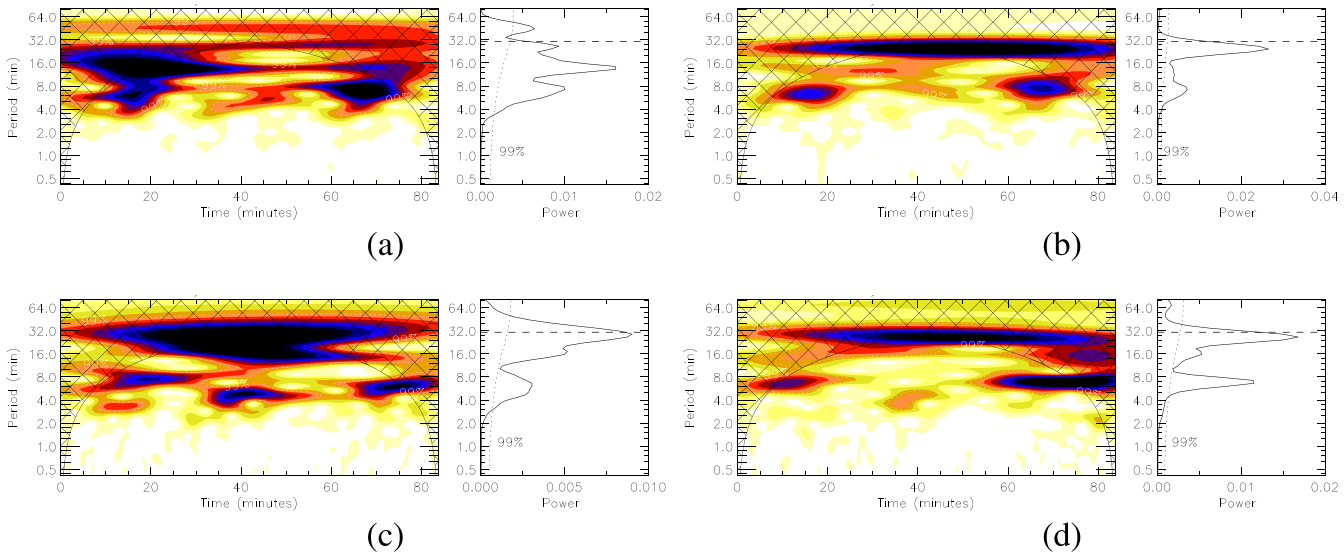

Figure 8. (a) Wavelet map and global wavelet of AIA 171 Å for slice 1 at position marked as dashed line in Figure 6. (b) Same as (a) for AIA 193 Å. (c) Wavelet map of AIA 171 Å for slice 2 at position marked as dashed line in Figure 6. (d) Same as (c) for AIA 193 Å.

Since the periodicity of ∼7 minutes is present in slices 0, 1, and 2, we create time–distance maps using Fourier filtered images. We perform a Fourier transform at each pixel location. Fourier power is then multiplied by a Gaussian peaking at 7 minutes with a FWHM of 1 minute and the inverse Fourier transform is applied to get the reconstructed light curve at the same pixel location. Fourier filtered movies of AIA 171 and 193 Å are available online as Movies 3 and 4, respectively. Time–distance maps for slices 1 and 2 using Fourier filtered images are shown in Figure 9. We find that the periodicity of ∼7 minutes is significant in AIA 193 Å and mostly toward the end of observation (from 60 to 80 minutes in Figure 9 lower right panel) at the position of slice 2. This is also evident from wavelet plots as shown in Figure 8 where we note that a periodicity of ∼7 minutes is present at the position of slice 2 at the start and toward the end of the observation from 60 to 80 minutes (see Figure 8(d)). This fact is also supported by Fourier filtered movie 4 where we see the significant PDs propagating outwards at the position of slice 2 toward the end of observation. A Similar behavior is found in AIA 171 Å wavelet plots in slices 1 and 2 but the presence of the 7 minutes periodicity at later times is most prominent in AIA 193 Å at the position of slice 2. This indicates that these PDs are triggered by some drivers at specific instances.

Since significant PDs are observed at later times at the position of slice 2, we fit the significant ridges with a straight line between 60 and 80 minutes in AIA 171 and 193 Å Fourier filtered time–distance maps for slit 2 as shown in Figure 9 right panel. The method of fitting is the same as explained in Section 2.3. We estimate the velocity to be $64 \pm 3\,\mathrm{km\,s^{-1}}$ ($73 \pm 3\,\mathrm{km\,s^{-1}}$) and $55 \pm 3\,\mathrm{km\,s^{-1}}$ ($79 \pm 2\,\mathrm{km\,s^{-1}}$) in AIA 171 Å (193 Å) for slices 1 and 2 respectively. We find that PDs of 7 minutes period are propagating with larger velocity in the hotter channel (AIA 193 Å), which further supports the fact that these could be propagating slow magnetoacoustic waves. However, we would like to point out that the PDs of 7 minutes period are not so clearly observed in AIA 171 Å and we see uneven ridges that could affect the velocity estimation. At the position of slice 1 (Figure 9 left panel) PDs of 7 minutes period are not clearly seen maybe because the period of 7 minutes is not the dominant one in the time series as shown in Figure 8(a). Thus we could fit only two ridges, one at 15 minutes and another at 65 minutes after the start of observation. We fit the corresponding ridges in AIA 193 Å and find that in slice 1, too, the velocity is higher in the hotter channel.

2.3.1. Jet-like Features in SJI 1300 Å

In this subsection we study the dynamic properties of the observed jet-like features. To determine the apparent speed of jets seen at the network boundary we place nine artificial box slices five pixels wide in SJI 1330 Å as shown in Figure 1(a). Slices are placed based on the direction of propagation of significant jets as seen in SJI 1330 Å in Movie 2 (available online). We average along the width of each box slice to increase signal to noise. Corresponding time–distance maps are

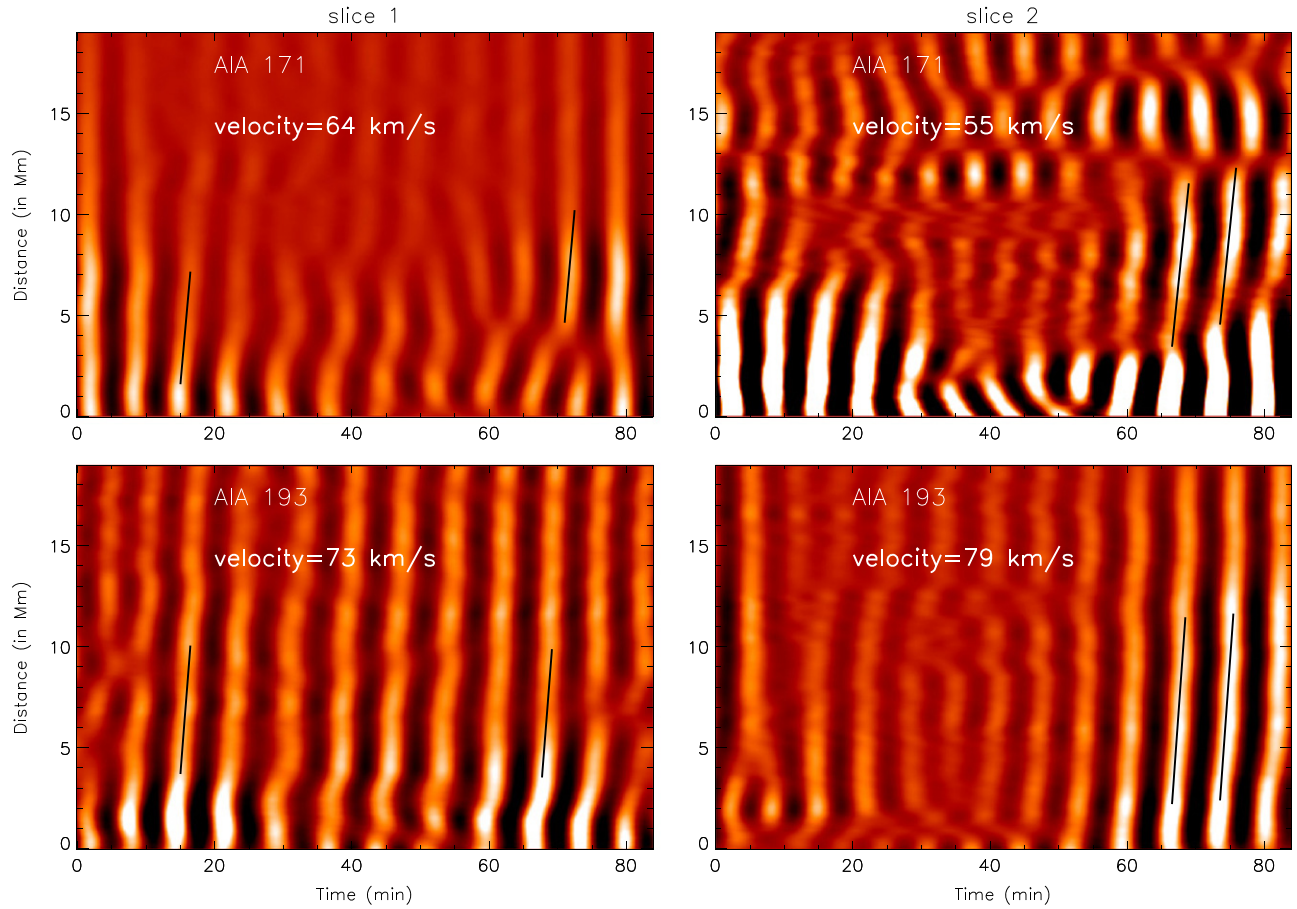

Figure 9. (Top panel) Left: *x–t* map at the position of slice 1; right: *x–t* map at the position of slice 2 as shown in Figure 1(c) using the 7 minutes Fourier filtered AIA 171 Å image overplotted with the best-fit straight line using the method mentioned in Section 2.3. (Bottom panel) Same as the top panel for AIA 193 Å.

(Animations a and b of this figure are available.)

shown in Figure 10. In the time–distance maps we fit significant ridges with straight lines. We find that several jets are preceded by brightenings seen in the time–distance maps, which suggests that small-scale reconnections could be triggering these jet-like features. We identify 62 jet-like features and fit them with dashed green curves as shown in Figure 10. The slope of the overplotted green dashed line gives an estimate of the apparent speed of the jet projected in the plane of sky. The velocity distribution of these jet-like features is shown in Figure 10 (last panel). We find that the distribution peaks around 10 km s^{-1}, which is similar to what has been reported by Shibata et al. (2007). Apart from outflows we see several downflows in the time–distance maps, which suggests that a certain amount of the jet material is falling back (see slit 4 in Figure 10).

2.3.2. Correspondence between Jet-like Features in SJI 1300 Å and PDs in AIA 171 and 193 Å

In this subsection we explore whether the jet-like features can be responsible for the generation of the PDs.

To understand the source of PDs generated in the corona, we compare the spectral intensity of *IRIS* slit spectra at the footpoint (marked by the triangle in Figure 1) and the intensity of PDs observed in the time–distance map of slit 0 (see Figure 6) at 2 Mm, which coincides with the position of the triangle marked in Figure 1, for AIA 171 Å and AIA 193 Å. The left panel of Figure 11 compares the peak intensity of *IRIS* slit spectra (top left), PDs (along slit 0) observed in AIA 171 Å (middle left), and PDs (along slit 0) observed in AIA 193 Å (bottom left). The dotted–dashed line in black represents the peak spectral intensity while the green line represents the corresponding intensity peaks in AIA 171 and 193 Å. We find that *IRIS* spectral intensity peaks precede the AIA intensity peaks and we estimate a lag of 24–84 s with a mean lag of ∼60 s.

Some of the peaks in spectral intensity do not correspond to sharp peaks in AIA 171 and 193 Å, maybe because the jet is aligned sideways, and do not move along the slice 0 placed co-spatially with the *IRIS* slit. We also compare the light curves at 0.5 Mm at box slice 8 placed in SJI 1330 Å (see Figure 1(a)) and 3 Mm at box slice 2 placed in AIA 171 and 193 Å (see Figures 1(c) and (d)). These two positions are also co-spatial.

From Figure 11, we note that there is fairly good one-to-one correspondence between jet-like features in slice 8 in *IRIS* SJI and PDs in slice 2 in AIA 171 and 193 Å. The dotted–dashed line represents the peak in *IRIS* SJI intensity. We also note that there is no significant lag except at the last ridge (marked by the dotted–dashed green line) where the lag is ∼120 s. We carry out a similar analysis for co-spatial positions at slice 3 placed in SJI 1330 Å and at slice 1 placed in AIA 171 and 193 Å. We found a lag of 84 s at two positions marked with green dotted–dashed lines.

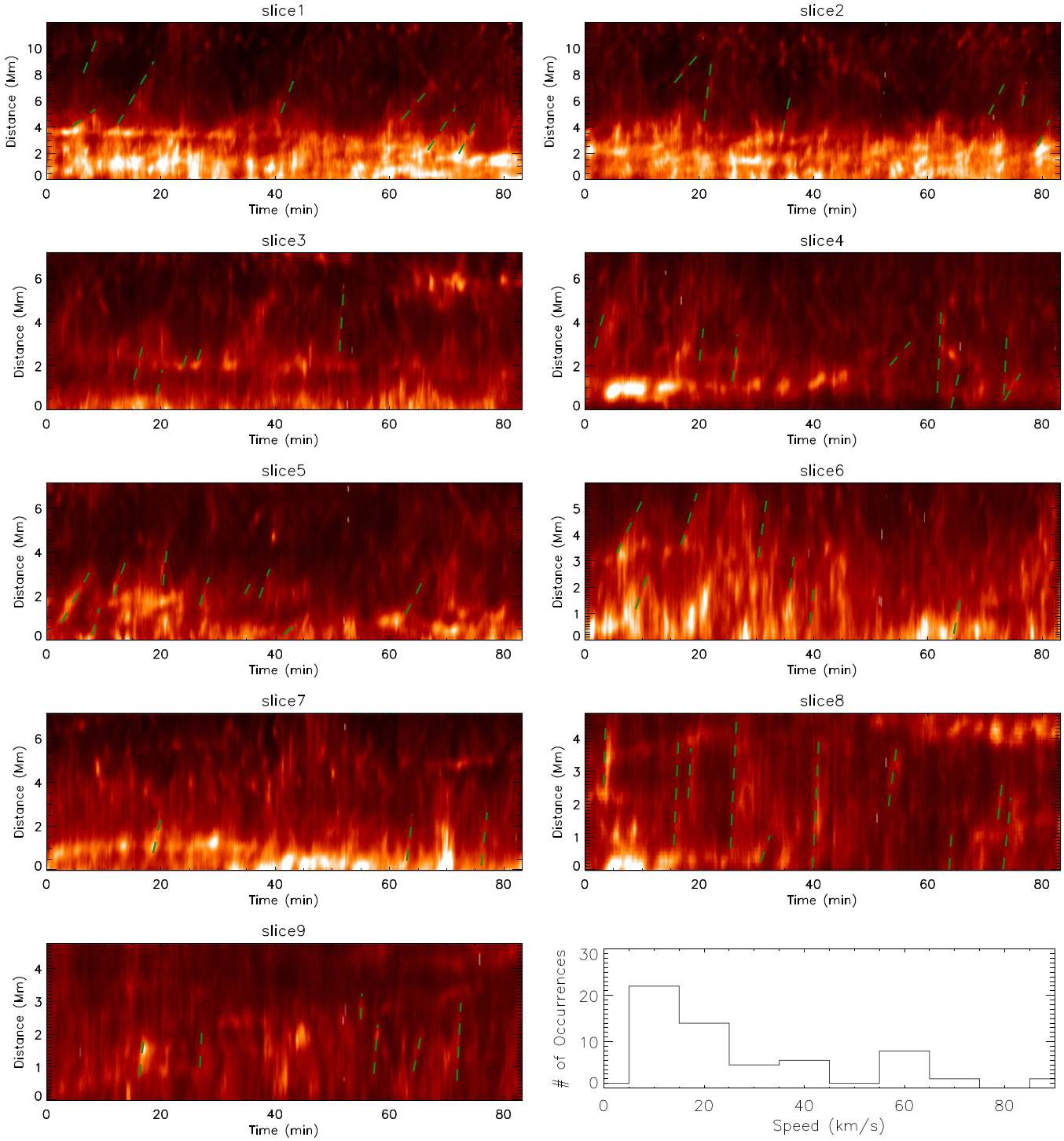

Figure 10. *x–t* maps for nine box slices as shown in Figure 1(a). The significant ridges in *x–t* maps are overplotted with dashed straight lines marked in green. The slope of the ridges gives an estimate of the velocity of the outward moving features (jet-like features). The distribution of jet apparent speeds is shown in the last panel. It peaks at 10 km s^{-1}.

It should be noted that the time lag between peaks in *IRIS* SJI and AIA is not uniform. Apart from the fact that some jets are preceded by the brightenings in *x–t* maps, at some positions we may not capture the exact time when a jet starts in *IRIS* SJI (see slice 8 in Figure 10 between 40 and 80 minutes). What we know is when a jet appears at the position of slices placed in *IRIS* SJI. It is also possible that when jets appear in a given slice, they have already covered some distance in the vertical direction (projection effect) and have generated the PDs visible in coronal channels. Thus they may appear co-temporal with PDs observed in AIA 171 and 193 Å.

These results allow us to propose that jet-like features in the transition region may cause PDs as observed in the corona.

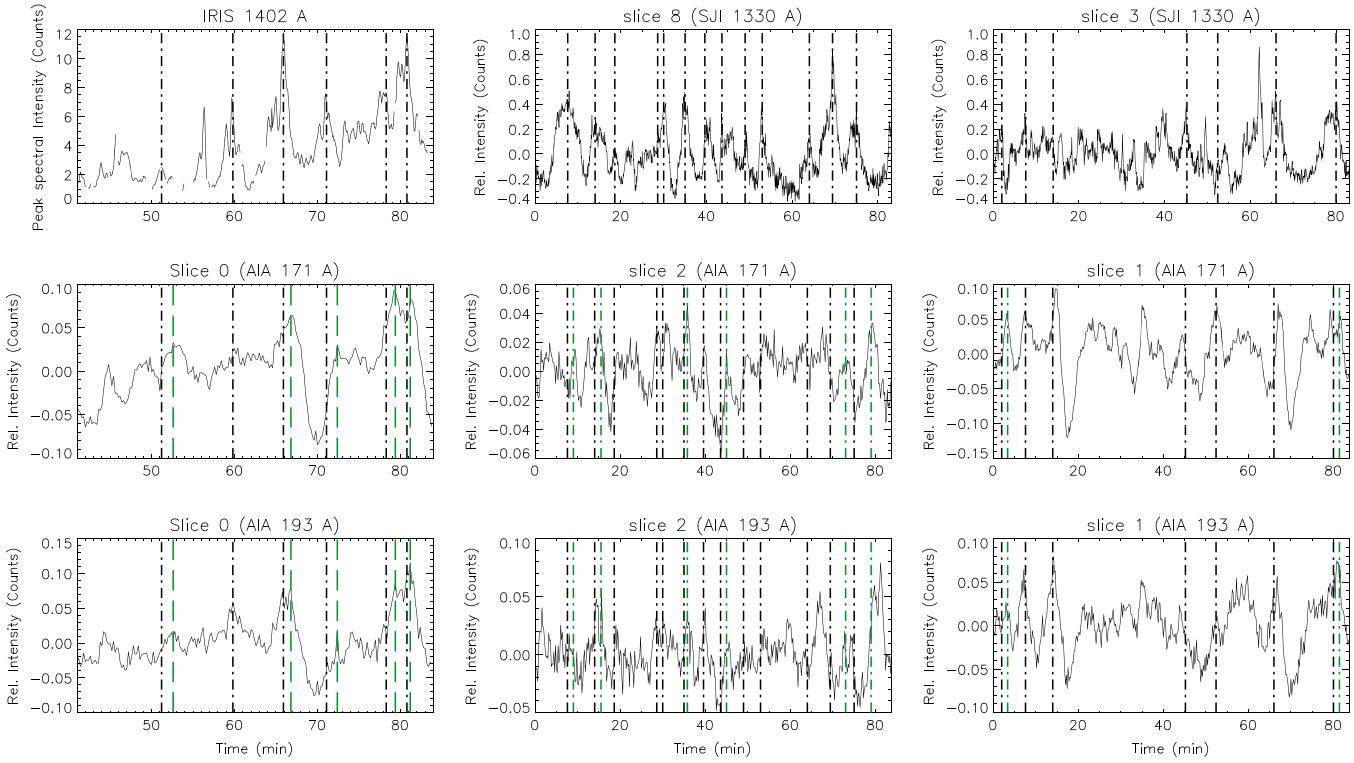

Figure 11. (Left panel)Top: *IRIS* spectral intensity at the position marked by the trangle in Figure 1. Middle: light curve of AIA 171 Å at the same position. Bottom: same as the middle panel but for AIA 193 Å. Black dotted–dashed lines correspond to the peak in spectral intensity. Green dotted–dashed lines mark the corresponding peaks in AIA 171 and 193 Å. The time lag can be estimated by estimating the time difference between the black and green lines. (Middle panel) Top: *IRIS* SJI 1330 Å light curve at 0.5 Mm for the *x*–*t* map created using box slice 8 as shown in Figure 10(a). Middle: AIA 171 Å light curve at 3 Mm (co-spatial with the position of the light curve of the top middle panel) for the *x*–*t* map created using box slice 2 in AIA 171 Å as shown in Figure 6 (top right panel). Bottom: AIA 193 Å light curve at 3 Mm for the *x*–*t* map created using slice 2 as shown in Figure 6 (bottom right panel). (Right panel) Same as the middle panel at a position co-spatial with slice 3 as shown in *IRIS* SJI and slice 1 in AIA 171 and 193 Å.

3. SUMMARY AND CONCLUSIONS

We study the dynamics at the footpoints of an on-disk plume adjacent to a coronal hole using combined imaging, spectroscopic and magnetic measurements. We find that there is continuous emergence of new magnetic flux of positive polarity (see Movie 1 online) and there is fairly good correspondence between intensity enhancement and the positive magnetic flux cancellation. This suggests that the emerging flux interacts with the existing fields, which results in reconnection and cancellation of the flux, resulting in small jet-like outflows termed "jetlets" as observed in AIA by Raouafi & Stenborg (2014). They conjectured that such small-scale jets are the consequences of flux cancellation at the footpoints of the plume. We think that jet-like features observed by Raouafi & Stenborg (2014) are the PDs that we observe in AIA channels. They associated the jetlets seen in AIA channels with the underlying magnetic flux change. In this article we report that underlying magnetic flux changes generate jet-like features, which trigger PDs in the corona. These PDs can be explained in terms of magnetoacoustic waves. The small-scale jets are quite evident in the *IRIS* 1330 Å SJIs (Movie 2 online) and the signature of reconnections is also prominent in the evolution of the line profiles. We observe enhanced line profile asymmetry, enhanced line width and large deviation from the average Doppler shift at specific instances. Association of plumes with supergranular network boundaries has been studied by several authors. In this study we find that plume footpoints coincide with network boundaries as seen in *IRIS* 1330 Å SJI. Observations of the origin of these jet-like features in connection with plumes are still lacking. In this article, we report observational evidence of the origin of jet-like features from network boundaries, thus confirming the earlier predictions. Footpoints of plumes are just enhanced network boundaries where we often see clear network jets in *IRIS* SJIs (Tian et al. 2014). The *IRIS* spectrum at a plume footpoint shows the presence of more than one Gaussian component, enhanced wings, high Doppler shifts and large fluctuations in intensity. This confirms the presence of flows (Tian et al. 2011a, 2012) at the footpoint of the plume. These jet-like features load mass into plumes.

We estimate the speed of the jet-like features by placing several slices in *IRIS* SJI. These jet-like features originate from network boundaries due to small-scale magnetic reconnections. We find that the speed distribution peaks at 10 kms^{-1}, which is the typical velocity for chromospheric anemone jets as reported by Shibata et al. (2007). Thus most of the jets could be chromospheric in origin. Recently, Rouppe van der Voort et al. (2015) have reported jets of similar velocity range seen in *IRIS* SJI 1330 Å to be associated with rapid blueshifted or redshifted excursions seen in Hα images. We find speeds of jets that are far lower than the 150 $\mathrm{km\,s}^{-1}$ reported in Tian et al. (2014). The datasets used by Tian et al. (2014) were centered on CHs while in this study the plume is located in a quiet Sun region. The open field lines in CHs may accelerate the jets to larger velocities. Apart from this, the effect of projection of jets in the plane of the sky cannot be ruled out.

We compared *IRIS* spectral intensity with PDs observed in AIA 171 and 193 Å and find that at several time instances the intensity enhancement in *IRIS* spectra precedes PDs observed in AIA channels. We found a lag of 24–84 s with a mean lag of 60 s. We also compared jet-like features in *IRIS* SJI with PDs observed in AIA channels at two different slice positions and find fairly good correspondence. However, at some instances we could not find one-to-one correspondence between *IRIS* SJI jet-like features and PDs observed in AIA channels. One reason could be that if jets are short-lived then they appear in *IRIS* SJIs but PDs in the corona may not be observed. We should point out that *IRIS* SJI 1330 Å has a strong contribution from C II which forms in the upper chromosphere. Thus *IRIS* SJI 1330 Å reflects the upper chromosphere and lower transition region, while emission in AIA 171 and 193 Å represents the million degree plasma. Thus if reconnection happens at larger heights (upper transition region or lower corona) and the plasma is heated to coronal temperatures then we may see faint jets in *IRIS* SJI but strong PDs in AIA channels. In addition to this, if observed jets do not propagate to greater heights, they may not be responsible for the generation of PDs in the corona. In the future, one can address this issue with better coordinated observations at several heights from chromosphere to corona. Therefore, we propose that there is some observational evidence that jet-like features at network boundaries may cause the generation of PDs in the corona.

Time–distance maps for AIA 171 and 193 Å reveal that the speed of quasi-periodic propagating intensity disturbances is larger in the hotter channel (AIA 193 Å) than in AIA 171 Å. Therefore, we believe that these are propagating slow magnetoacoustic waves. Ofman et al. (2012) reported that the impulsive onset of flows with subsonic speed results in excitation of damped slow magnetoacoustic waves in active region loops. Wang et al. (2013) performed 3D MHD modeling of active region fan loops and report that the PDs observed in coronal fan loops are due to several tiny upflows caused by nanoflares at the loop footpoints. Nishizuka & Hara (2011) reported the presence of flows close to the footpoint and upward propagating slow magnetoacoustic waves at higher locations using EIS on board *Hinode*. Thus it appears that any form of reconnection outflow may generate slow waves in an expanding loop system. In this study, we report that the periodicities of intensity disturbances found in the corona using AIA 171 and 193 Å match well with periodicities found in *IRIS* spectral intensity and in *IRIS* SJI intensity in the transition region. Therefore, some jets observed in the transition region may be connected to PDs observed in the corona. This fact, together with the good correspondence between some jet-like features in *IRIS* images and some PDs in AIA coronal passbands, allows us to propose that the small jet-like upflows (jetlets) at lower heights (the transition region) are the drivers of slow magnetoacoustic waves seen at coronal heights in plumes.

We thank the *IRIS* team for providing the data in the public domain. We thank Dr. Hui Tian for his valuable suggestions, which have enabled us to improve the manuscript. We also thank the anonymous referee for careful reading and constructive suggestions. *IRIS* is a NASA small explorer mission developed and operated by LMSAL with mission operations executed at NASA Ames Research Center and major contributions to downlink communications funded by the Norwegian Space Center (NSC, Norway) through an ESA-PRODEX contract. We acknowledge partial support from the Belgian Federal Science Policy Office through the ESA-PRODEX program.

REFERENCES

Banerjee, D., O'Shea, E., & Doyle, J. G. 2000, SoPh, 196, 63
Banerjee, D., O'Shea, E., Doyle, J. G., & Goossens, M. 2001, A&A, 377, 691
Banerjee, D., Teriaca, L., Gupta, G. R., et al. 2009, A&A, 499, L29
De Pontieu, B., McIntosh, S. W., Hansteen, V. H., & Schrijver, C. J. 2009, ApJL, 701, L1
De Pontieu, B., Title, A. M., Lemen, J. R., et al. 2014, SoPh, 289, 2733
DeForest, C. E., & Gurman, J. B. 1998, ApJL, 501, L217
DeForest, C. E., Hoeksema, J. T., Gurman, J. B., et al. 1997, SoPh, 175, 393
DeForest, C. E., Lamy, P. L., & Llebaria, A. 2001, ApJ, 560, 490
Dolla, L. R., & Zhukov, A. N. 2011, ApJ, 730, 113
Fisher, R., & Guhathakurta, M. 1995, ApJL, 447, L139
Gary, G. A. 1989, ApJS, 69, 323
Grappin, R., Wang, Y.-M., & Pantellini, F. 2011, ApJ, 727, 30
Gupta, G. R., O'Shea, E., Banerjee, D., Popescu, M., & Doyle, J. G. 2009, A&A, 493, 251
Harvey, J. W. 1965, ApJ, 141, 832
Huang, Z., Madjarska, M. S., Xia, L., et al. 2014, ApJ, 797, 88
Kiddie, G., De Moortel, I., del Zanna, G., McIntosh, S. W., & Whittaker, I. 2012, SoPh, 279, 427
Krishna Prasad, S., Banerjee, D., van Doorsselaere, T., & Singh, J. 2012, A&A, 546, A50
Lemen, J. R., Title, A. M., Akin, D. J., et al. 2012, SoPh, 275, 17
Madjarska, M. S., Doyle, J. G., & De Pontieu, B. 2009, ApJ, 701, 253
McIntosh, S. W., Innes, D. E., De Pontieu, B., & Leamon, R. J. 2010, A&A, 510, L2
Newkirk, G., Jr., & Harvey, J. 1968, SoPh, 3, 321
Nishizuka, N., & Hara, H. 2011, ApJL, 737, L43
Ofman, L., Romoli, M., Poletto, G., Noci, G., & Kohl, J. L. 1997, ApJL, 491, L111
Ofman, L., Wang, T. J., & Davila, J. M. 2012, ApJ, 754, 111
O'Shea, E., Banerjee, D., & Doyle, J. G. 2006, A&A, 452, 1059
Raouafi, N.-E., Harvey, J. W., & Solanki, S. K. 2006, Lacoste, H. in ESA Special Publication 617, *SOHO*-17. 10 Years of *SOHO* and Beyond, (Nordwijk: ESTEC), 16
Raouafi, N.-E., Harvey, J. W., & Solanki, S. K. 2007, ApJ, 658, 643
Raouafi, N.-E., Petrie, G. J. D., Norton, A. A., Henney, C. J., & Solanki, S. K. 2008, ApJL, 682, L137
Raouafi, N.-E., & Stenborg, G. 2014, ApJ, 787, 118
Rouppe van der Voort, L., De Pontieu, B., Pereira, T. M. D., Carlsson, M., & Hansteen, V. 2015, ApJL, 799, L3
Saito, K. 1958, PASJ, 10, 49
Saito, K. 1965, PASJ, 17, 1
Saito, K., & Tanaka, Y. 1957, PASJ, 9, 106
Schou, J., Scherrer, P. H., Bush, R. I, et al. 2012, SoPh, 275, 229
Shibata, K., Nitta, N., Strong, K. T., et al. 1994, ApJL, 431, L51
Shibata, K., Nakamura, T., Matsumoto, T., et al. 2007, Sci, 318, 1591
Tian, H., DeLuca, E. E., Cranmer, S. R., et al. 2014, Sci, 346, 1255711
Tian, H., McIntosh, S. W., & De Pontieu, B. 2011a, ApJL, 727, L37
Tian, H., McIntosh, S. W., De Pontieu, B., et al. 2011b, ApJ, 738, 18
Tian, H., McIntosh, S. W., Habbal, S. R., & He, J. 2011c, ApJ, 736, 130
Tian, H., McIntosh, S. W., Wang, T., et al. 2012, ApJ, 759, 144
Torrence, C., & Compo, G. P. 1998, BAMS, 79, 61
van de Hulst, H. C. 1950, BAN, 11, 150
Velli, M., Lionello, R., Linker, J. A., & Mikić, Z. 2011, ApJ, 736, 32
Verwichte, E., Marsh, M., Foullon, C., et al. 2010, ApJL, 724, L194
Wang, T., Ofman, L., & Davila, J. M. 2013, ApJL, 775, L23
Wang, Y.-M., & Muglach, K. 2008, SoPh, 249, 17
Wang, Y.-M., & Sheeley, N. R., Jr. 1995, ApJ, 452, 457
Wilhelm, K., Abbo, L., Auchère, F., et al. 2011, A&ARv, 19, 35
Young, P. R., Klimchuk, J. A., & Mason, H. E. 1999, A&A, 350, 286